Research Article

Elucidating the stability of ligand-protected Au nanoclusters under electrochemical reduction of CO_2

Anantha Venkataraman Nagarajan[1] · Rosalba Juarez-Mosqueda[1] · Michael J. Cowan[1] · Rongchao Jin[2] · Douglas R. Kauffman[3] · Giannis Mpourmpakis[1]

Abstract

Ligand-protected gold nanoclusters are a novel class of particles that have attracted great interest in the field of catalysis due to their atomically-precise structure, high surface-to-volume ratio, and unique electronic properties. In particular, the anionic thiolate-protected Au_{25} nanocluster (NC), $[Au_{25}(SR)_{18}]^{1-}$, with partially lost ligands, has been demonstrated to act as an active catalyst for the electrochemical reduction of CO_2. However, the stability of this and other thiolate-protected NCs after partial ligand removal remains elusive. Using density functional theory (DFT) calculations and the recently developed thermodynamic stability model, we investigate the stability of $[Au_{25}(SR)_{18}]^{1-}$, $[Au_{18}(SR)_{14}]^0$, $[Au_{23}(SR)_{16}]^{1-}$, and $[Au_{28}(SR)_{20}]^0$ with ligand loss. Additionally, we examine the stability of the partially protected NCs upon adsorption of CO_2 reduction reaction intermediates (i.e. H, CO, and COOH) on the different active sites generated after ligand removal. Our results reveal that the partially protected Au_{25} NC shows the highest stability compared to the other partially protected NCs in the presence of electrochemical reduction intermediates. We find that the presence of the COOH intermediate on the generated active sites stabilizes the Au_{25} NC almost as well as the removed ligands. Moreover, time-dependent DFT calculations and UV–Vis/Raman experiments suggest that the most probable ligand removal mode under electrochemical conditions is the one that generates S active sites, in agreement with the DFT ligand removal thermodynamic analysis. Importantly, this study demonstrates the robustness of the Au_{25} NC and offers a novel way to address stability of ligand protected NCs during electrocatalytic reaction conditions.

Keywords First principles calculations · Electrocatalysis · Optical spectra · Reaction intermediates

1 Introduction

Atomically precise thiolate-protected gold nanoclusters (NCs) are a fascinating class of nanoparticles (< 3 nm in diameter) [1] that display molecular-like physicochemical properties [2–5]. They are commonly represented by the $[Au_n(SR)_m]^q$ formula, where n denotes the number of gold atoms, m is the number of stabilizing thiolate ligands and q is the total charge [5]. Since the first report on the crystallization and X-ray structure determination of the $Au_{102}(SR)_{44}$ NC [6], the stability of Au ligand-protected NCs has been broadly investigated leading to important concepts that, up to some extent, explain their remarkable stability in terms of the electronic shell closure arguments [7–9] . Recently, Taylor et al. developed the thermodynamic stability model (TSM) capable of explaining

the stability of a large series of experimentally synthesized metal NCs, among which were NCs that do not fall into the classification of electronic shell-closing structures (or superatomic clusters) [8, 10, 11]. This model is based on the balance between the shell-to-core binding energy (SCBE) and core cohesive energy (CE) of the nanocluster investigated through first-principles calculations [11]. In the TSM model, the SCBE describes the energetic interaction between the shell of the metal NC and its core, while the core CE describes the energetic interaction of the metal atoms within the core. Thus, the balance between the SCBE and core CE determines the stability of a NC.

The inherent stability exhibited by ligand protected NCs, along with their high surface-to-volume ratio, their precisely known surface structure, and discrete electronic states have made these NCs attractive functional materials for applications in catalysis [12–25], with the Au_{25} NC being the most investigated NC for this purpose. Experimental and computational studies have demonstrated that the Au_{25} NC exhibits exceptional catalytic behavior for the oxidation of styrene, CO, the hydrogenation of ketones and aldehydes, photocatalytic water splitting, and more recently, the electrochemical reduction of CO_2 [14, 16, 18, 20–22, 25–31] . In a series of experimental and computational studies, Kauffman et al. have investigated the electrochemical reduction of CO_2 to CO using the $[Au_{25}(SR)_{18}]^{1-}$ NC as a catalyst [12, 22, 26, 31]. They reported that the electrochemical reduction of CO_2 to CO arises from the reversible electronic interaction between the fully-protected $[Au_{25}SR_{18}]^{1-}$ NC and CO_2, and the subsequent charge redistribution within the $[Au_{25}SR_{18}]^{1-}$ NC [26]. In addition, a remarkable stability of $[Au_{25}(SR)_{18}]^{1-}$ NC was demonstrated through a multi-day (36 h) CO_2 electrochemical reduction experiment containing multiple start/stop cycles [22].

Furthermore, density functional theory (DFT) calculations have demonstrated that in order for the $[Au_{25}(SR)_{18}]^{1-}$ NC to catalyze the CO_2 reduction, the exposure of either a metal atom or sulfur atom on the surface of the NC is crucial [17, 21]. Based on DFT calculations, Alfonso et al., and Austin et al., have independently shown that the de-thiolated surface Au site in the Au_{25} NC plays an important role in stabilizing the carboxyl intermediate formed during the electrochemical reduction of CO_2 [21, 31]. Moreover, the formation of the COOH intermediate has been found to be the most endergonic step in the reaction pathway [31]. The results of Austin et al. also suggest that the exposure of a S atom, generated after –R ligand removal, is thermodynamically more favorable and more selective for the CO_2 reduction than having an exposed Au atom on the NC surface from a –SR ligand removal. With thiolate-protected Au NCs being stable due to the presence of ligands on their surface, but also active for CO_2 reduction due to ligand loss, an important question
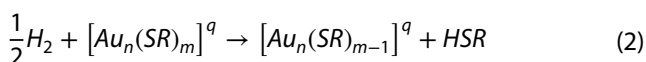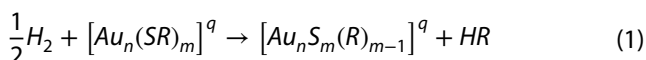
emerges: How can the ligand protected Au NCs be stable under electrochemical reduction conditions when they lose surface ligands?

In this work, we use DFT calculations to investigate the effect of the –R or –SR ligand removal from the capping layer of $[Au_{18}(SR)_{14}]^0$, $[Au_{23}(SR)_{16}]^{1-}$, $[Au_{25}(SR)_{18}]^{1-}$, and $[Au_{28}(SR)_{20}]^0$ NCs. Particularly, we analyze the thermodynamic stability of the four fully and partially protected ligand protected NCs using the TSM [11]. Furthermore, we gain insights into the stability of partially protected NCs upon adsorption of CO, COOH and H intermediates, formed during the electrochemical reduction of CO_2. Finally, we use TDDFT to report absorption features of the $[Au_{25}(SR)_{18}]^{1-}$ NC when ligands have been replaced by CO_2 reduction reaction intermediates and compare with experimental absorption spectra.

2 Computational methods

Electronic structure calculations were performed within the framework of DFT using the Perdrew-Burke-Ernzerhof (PBE) functional [32] and the double-zeta valence polarized (DZVP) basis set with a cutoff of 500 Ry in combination with Goedecker-Teter-Hutter (GTH) pseudopotentials [33]. The calculations were performed in the computational package CP2K [4, 34]. The initial geometries of the $[Au_{18}(SR)_{14}]^0$, $[Au_{23}(SR)_{16}]^{1-}$, $[Au_{25}(SR)_{18}]^{1-}$, and $[Au_{28}(SR)_{20}]^0$ NCs were obtained from reported crystal structures [35–38]. Unless explicitly mentioned, the –R groups were replaced with $–CH_3$ ligands to reduce computational cost. Replacing the full organic groups by methyl groups has shown to have minimal effect on the catalytic properties of $Au_n(SR)_m$ NCs while the nanocluster core maintains its structural integrity [12, 17, 21, 22, 26, 29, 31, 39, 40]. The structure optimizations were performed using a non-periodic cell of dimensions 32 Å × 32 Å × 32 Å until the forces were less than 0.002 eV Å^{-1}.

The energy to remove a –R or –SR ligand from the thiolate-protecting layer of the $[Au_n(SR)_m]^q$ nanoclusters was calculated as the difference between the electronic energies of product and reactants based on the following reactions:

$$\frac{1}{2}H_2 + [Au_n(SR)_m]^q \rightarrow [Au_nS_m(R)_{m-1}]^q + HR \quad (1)$$

$$\frac{1}{2}H_2 + [Au_n(SR)_m]^q \rightarrow [Au_n(SR)_{m-1}]^q + HSR \quad (2)$$

$$\Delta E = E_{products} - E_{reactants} \quad (3)$$

In these reactions, either a –R (Eq. 1) or –SR (Eq. 2) group is removed to generate an exposed S or Au site on the NC

surface, respectively. E in Eq. (3) represents the total electronic energy of the respective species. The ligand removal in ligand protected NCs and metal surfaces under reaction conditions has been reported earlier [12, 17, 21, 22, 26, 29, 31, 39–41]. The stability of the partially protected NCs was assessed by calculating the deviation from the parity line and comparing it against that of the corresponding fully protected NCs (Eq. 4). The parity is the balance between the SCBE and core CE which in turn determines the thermodynamic stability of the ligand protected NCs as stated in the TSM [11]. The same approach was used to determine the stability of the NCs when different intermediates of the CO_2 reduction reaction (H, COOH and CO) were present on either the generated S or Au sites of the NC.

$$\text{Deviation from parity} = \frac{\text{SCBE} - \text{Core CE}}{\sqrt{2}} \quad (4)$$

Furthermore, the photo-absorption spectra of the fully thiolate-protected $[Au_{25}(SR)_{18}]^{1-}$ NC and the adsorbate-thiolate-protected Au_{25} complexes (i.e. $[Au_{25}SH(SR)_{17}]^{1-}$, $[Au_{25}SCOOH(SR)_{17}]^{1-}$, $[Au_{25}H(SR)_{17}]^{1-}$, $[Au_{25}COOH(SR)_{17}]^{1-}$, and $[Au_{25}CO(SR)_{17}]^{1-}$) were calculated within the framework of time-dependent DFT (TDDFT). The structural optimizations and TDDFT calculations were performed using the PBE [32] functional and a real-space grid with spacing of 0.2 Å in GPAW [42, 43].

3 Experimental methods

The synthesis of $[Au_{25}(PET)_{18}]^{1-}$ (PET = phenylethanethiolate, counterion = tetraoctylammonium) followed a previously reported approach [29]. Electrochemical experiments were performed using a Biologic SP150 potentiostat and Ag/AgCl reference, glassy carbon (GC) working, and Pt wire counter electrodes. The reference electrode was calibrated against a commercially available reversible hydrogen electrode (RHE; Gasketell Hydroflex). $[Au_{25}(PET)_{18}]^{1-}$ nanoclusters were dissolved in acetone, dropcast directly onto the GC electrode, and allowed to dry in air. The electrode was held at a potential of − 1 V versus RHE in CO_2 saturated 0.1 M $KHCO_3$ for 1 h to expose the nanoclusters to electrochemical CO_2 reduction conditions. We did not use carbon black or other catalyst supports to facilitate post-reaction Raman spectroscopy of $[Au_{25}(PET)_{18}]^{1-}$ nanoclusters directly on the electrode surface and to allow dissolution of Au_{25} nanoclusters back into solvent after CO_2 reduction for UV–Vis absorption spectroscopy measurements.

UV–Vis absorption spectra were collected using an Agilent 8453 spectrophotometer by dissolving $[Au_{25}(PET)_{18}]^{1-}$ nanoclusters in dimethylformamide solvent. The collected wavelength-dependent absorption intensities, $I(w)$, were converted into energy-dependent absorption intensity, $I(E)$, using the following relationship to conserve the energy-dependent spectral peak areas for comparison with predicted optical absorption spectra: $I(E) = I(w)\left(\frac{\partial E}{\partial W}\right) \propto I(w) \times w^2$, where $\left(\frac{\partial E}{\partial W}\right)$ is the so-called Jacobian factor [1, 44, 45]. The UV–Vis absorption spectra were normalized to a value of 1.0 at 3.45 eV and offset for clarity. Raman spectra were collected with a Horiba LabRam HR-Evolution spectrometer using a 100 × objective, 785 nm laser, and a 5% neutral density filter. Low laser intensity was used to prevent sample damage, and the reported spectra were averaged over at least three different locations on the sample. Raman spectra of $[Au_{25}(PET)_{18}]^{1-}$ nanoclusters before CO_2 reduction reaction were collected by scraping a small amount of solid nanocluster sample onto a glass slide. Raman spectra of $[Au_{25}(PET)_{18}]^{1-}$ nanoclusters after electrochemical CO_2 reduction were collected with nanoclusters remaining on the GC electrode. A non-linear background was subtracted from all Raman spectra using the instrument software, spectral intensities were normalized to 1.0 at peak intensity (291 cm^{-1}), and the spectra were offset for clarity.

4 Results and discussion

We first geometrically optimize the structures of $[Au_{18}(SR)_{14}]^{0}$, $[Au_{23}(SR)_{16}]^{1-}$, $[Au_{25}(SR)_{18}]^{1-}$, and $[Au_{28}(SR)_{20}]^{0}$, where R=CH₃, using DFT. The four ligand protected NCs were selected due to their similar size (core size of ~ 1 nm) and similar protecting staple motifs (i.e. Au–SR-Au units). All four NCs have been experimentally synthesized and structurally characterized [35–38]. In Fig. 1, we show the optimized structures and indicate the specific sites of ligand removal. While the sites between the different NCs are not completely identical, we believe that the local chemical environment surrounding the staple motifs is similar enough to warrant comparison. As a case study, we have studied this aspect for the $[Au_{25}(SR)_{18}]^{1-}$ NC (see Fig. S1 and S2) Owing to the overall symmetry of the $[Au_{25}(SR)_{18}]^{1-}$ NC, there are two possible distinct sites for –R or –SR removal. The energetics for ligand removal from these sites has been included in the SI of the manuscript and we see that the difference between removing the –SR group from the two sites is less than 4 kcal/mol.

Using the optimized structures, we next calculate the ligand removal energies for the four ligand-protected NCs, as shown in Fig. 2. Our results reveal that removing a –R group from any of the ligand-protected NCs is thermodynamically more favorable than removing a full thiol group,
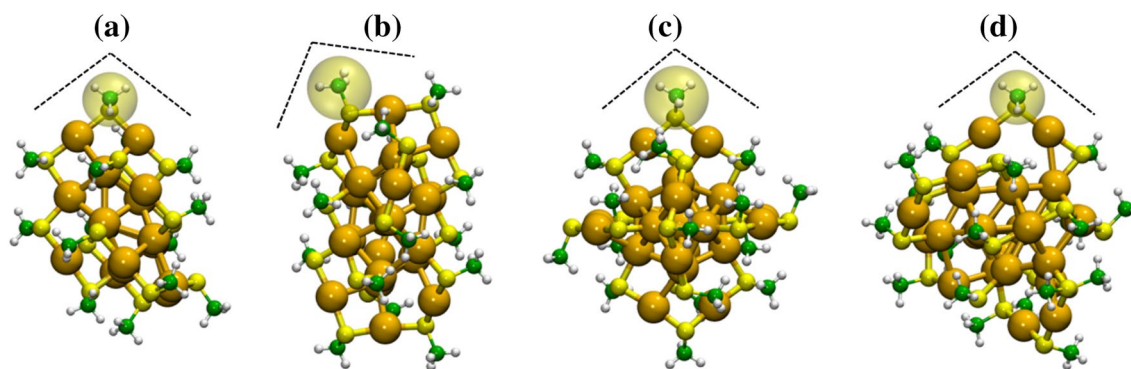
Fig. 1 Optimized $[Au_n(SR)_m]^q$ nanoclusters: **a** $[Au_{18}(SR)_{14}]^0$, **b** $[Au_{23}(SR)_{16}]^{1-}$, **c** $[Au_{25}(SR)_{18}]^{1-}$, and **d** $[Au_{28}(SR)_{20}]^0$. The dashed lines indicate the Au–SR–Au units and the yellow circles indicate the sites of ligand removal. Orange, yellow, green, and white spheres represent the Au, S, C and H atoms, respectively
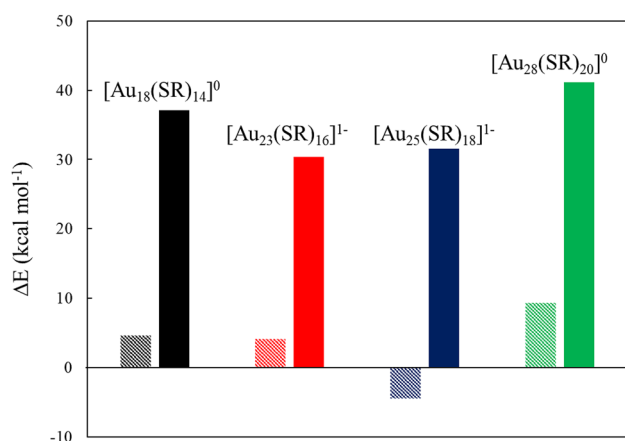

Fig. 2 Change in electronic reaction energy (ΔE) for a single ligand –R (striped bars) or –SR removal (solid bars) from $[Au_n(SR)_m]^q$ nanoclusters (with R=CH$_3$). ΔE values (in kcal mol^{-1}) are calculated based on hydrogenation reactions of Eqs. 1 and 2

Fig. 3 Parity plot between the shell-to-core binding energy (SCBE) and core cohesive energy (CE) upon –R or –SR removal. Circles, squares, and triangles indicate the SCBE-CE of the original $[Au_n(SR)_m]^q$, the $[Au_nS(SR)_{m-1}]^q$ and the $[Au_n(SR)_{m-1}]^q$ NCs respectively. Black, red, blue, and green colors are used to identify the fully and partially protected Au_{18}, Au_{23}, Au_{25}, and Au_{28} NCs, respectively

which agrees with previous work [46]. Furthermore, we found that removing a –R group from $[Au_{25}(SR)_{18}]^{1-}$ is more favorable (− 4.43 kcal mol^{-1}) compared to $[Au_{18}(SR)_{14}]^0$ (4.64 kcal mol^{-1}), $[Au_{23}(SR)_{16}]^{1-}$ (3.10 kcal mol^{-1}), and $[Au_{28}(SR)_{20}]^0$ (9.38 kcal mol^{-1}). We note that the ΔE value for –R removal from the $[Au_{25}(SR)_{18}]^{1-}$ is negative. However, this does not mean that the –R group will spontaneously desorb from the surface since we would expect a kinetic barrier limiting this process. However, we expect –R removal to occur under electrochemical (reaction) conditions where a potential is applied such that the system is not limited by the kinetic barrier and is instead controlled by thermodynamics. Additionally, it is worth noting that the energies reported in this work are electronic energies and due to the fact that we simulate all the R-ligands with methyl groups, we inherently screen the effect of the NC shape, size (these NCs are close in size, but differ on the number of Au atoms and ligands) and charge on the R–S
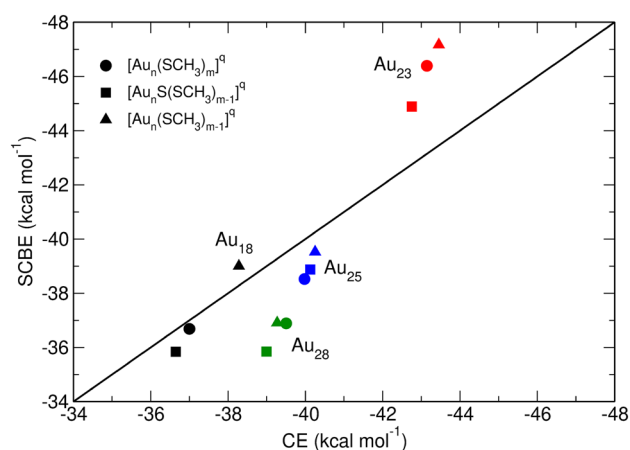
and Au–S bond dissociation. Although we do not account for entropic effects considering full ligands (calculations of extremely high computational cost) of the NCs, the results in Fig. 2, clearly indicate that from a thermodynamics perspective it is easier to break the R–S bond than the S–Au bond of the NCs.

We used the TSM and plotted the SCBE against core CE to examine the stability of the four $[Au_n(SR)_m]^q$ NCs and their partially protected counterparts (Fig. 3). The deviation from parity is calculated as mentioned in the computational methods section. We find that the fully and partially protected Au_{25} and Au_{18} NCs show approximately a 1:1 parity between the SCBE and core CE, demonstrating their overall robustness and tendency to maintain the energy balance even with ligand removal. Although the
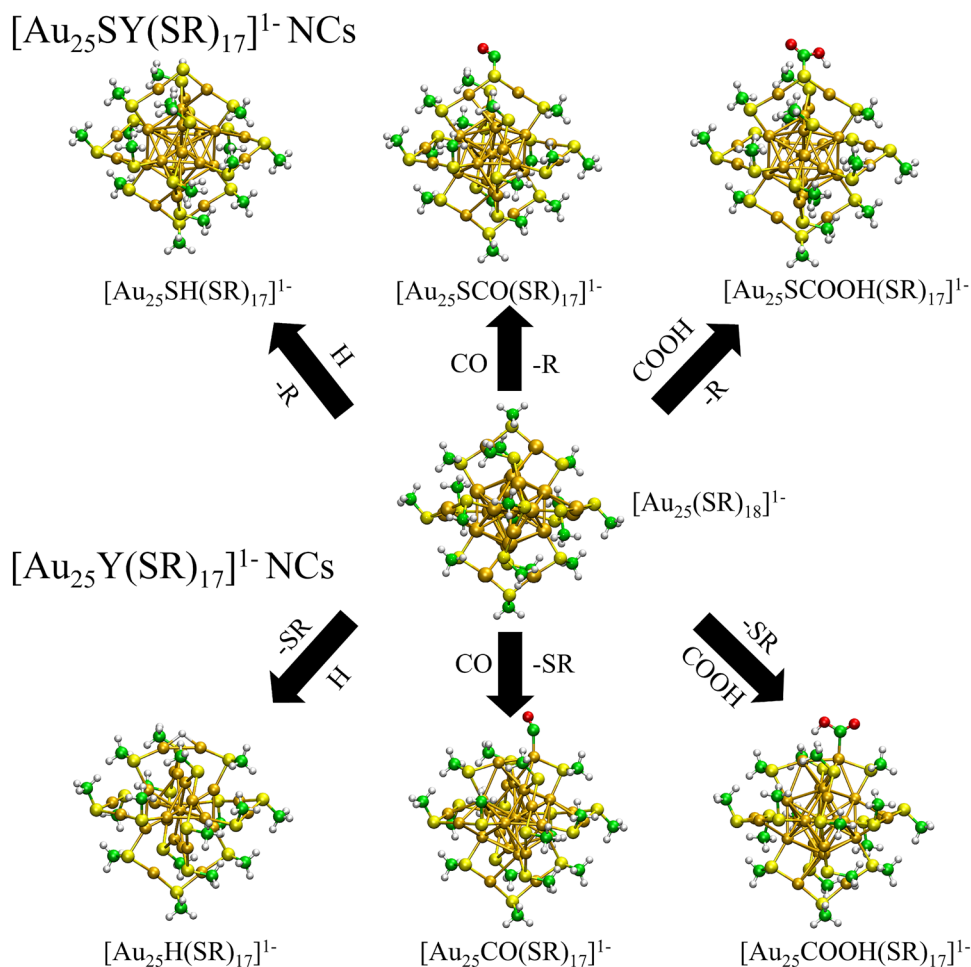
fully protected Au_{23} and Au_{28} NCs seem to exhibit deviation from the parity they still fall within the limit of stability as per the TSM [11]. The deviation from the parity for the cases of Au_{23} and Au_{28} NCs (both fully and partially protected) is approximately 1 kcal mol^{-1} larger than those for the Au_{18} and Au_{25} NCs. Overall, according to the relative changes in parity, we expect the partially protected Au_{25} NC to show higher stability as compared to the other partially protected NCs (all Au_{25} points fall close to the parity and cluster together demonstrating energy balance robustness going from fully to partial protected NC).

Next, we analyze the stability of the partially protected $[Au_nS(SR)_{m-1}]^q$ and $[Au_n(SR)_{m-1}]^q$ NCs when an adsorbate is bound to the exposed S or Au active sites. We chose to study H, CO, and COOH as adsorbates since they have been observed as intermediates during the electrochemical reduction of CO_2 to CO [12, 22, 26, 31]. With three adsorbates and two possible active sites from ligand removal, we have a total of six possible configurations for each ligand protected NC. These resulting structures are depicted for the $[Au_{25}(SR)_{18}]^{1-}$ NC in Fig. 4. $[Au_{25}SY(SR)_{17}]^{1-}$ denotes the partially protected Au_{25} NC with an adsorbate (Y) present on the S-exposed site, whereas, $[Au_{25}Y(SR)_{17}]^{1-}$ denotes the partially protected Au_{25} NC with an adsorbate (Y) on the Au-exposed site.

The effect of the adsorbates on the stability of the adsorbate-thiolate-protected $[Au_nSY(SR)_{m-1}]^q$ or $[Au_nY(SR)_{m-1}]^q$ NCs (with Y being the H, CO, or COOH molecule adsorbed on the generated S or Au active sites of the NCs) was examined through the TSM [11]. The deviation from parity for the adsorbate-thiolate-protected NCs was calculated and compared to the deviation from parity for their corresponding fully protected NC. The results plotted in Fig. 5 show that the maximum deviation from the parity is exhibited by the Au_{23} and Au_{28} NCs while minimum deviation is exhibited by the Au_{18} and Au_{25} NCs. These results are similar to the trend observed for ligand removal. This implies that the adsorbates present on the S or Au exposed sites do not drastically change the SCBE or core CE energy of the NCs. This is consistent with our observation of no significant structural rearrangement of the NCs during geometry optimization. From Fig. 5a, it can be observed that with the exception of CO on the Au active site, the deviation from the parity displayed by the

Fig. 4 Schematic depicting the adsorption of the reaction intermediates (Y = H, CO or COOH) on the generated Au or S exposed site using the $[Au_{25}(SR)_{18}]^{1-}$ NC as an example. The structures correspond to optimized geometries

$[Au_{25}SY(SR)_{17}]^{1-}$ NCs

$[Au_{25}SH(SR)_{17}]^{1-}$ $[Au_{25}SCO(SR)_{17}]^{1-}$ $[Au_{25}SCOOH(SR)_{17}]^{1-}$

$[Au_{25}(SR)_{18}]^{1-}$

$[Au_{25}Y(SR)_{17}]^{1-}$ NCs

$[Au_{25}H(SR)_{17}]^{1-}$ $[Au_{25}CO(SR)_{17}]^{1-}$ $[Au_{25}COOH(SR)_{17}]^{1-}$
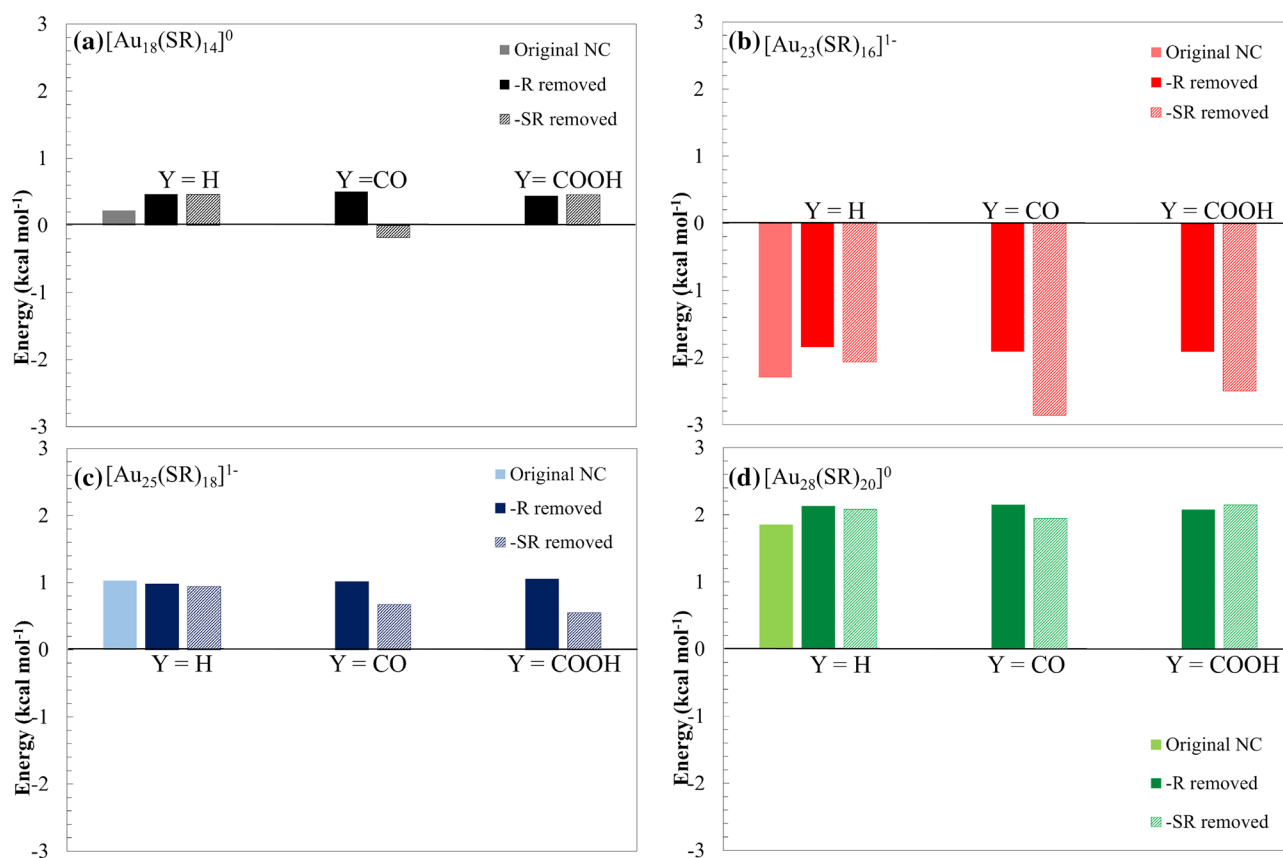
Fig. 5 Deviation of the adsorbate-thiolate-protected $[Au_nSY(SR)_{m-1}]^q$ and $[Au_nY(SR)_{m-1}]^q$ NCs from parity compared to that of the original $[Au_n(SR)_m]^q$ NC. Solid bars represent the deviation when the adsorbate is present on the S active site $[Au_nSY(SR)_{m-1}]^q$, whereas striped bars represent the deviation when the adsorbate is present on the Au active site $[Au_nY(SR)_{m-1}]^q$

adsorbate-thiolate-protected Au_{18} NCs slightly increases, thus implying relatively lower stability as compared to the fully protected Au_{18} NCs. We observe a similar trend for the adsorbate-thiolate-protected Au_{28} NCs (Fig. 5d), wherein the adsorption of the intermediates on the S or Au active site slightly increases the deviation from parity and relative stability with respect to the original fully protected Au_{28} NC. Figure 5b shows the deviation of the adsorbate-thiolate-protected Au_{23} NC from parity. We observe that when the CO and COOH intermediates are present on the Au active site, the deviation from parity is increased which implies a decrease in the relative stability compared to the original Au_{23} NC. It is worth noting that in all other cases, the presence of adsorbates decreases the distance from parity for the adsorbate-thiolate-protected Au_{23} NC. In contrast, the adsorbate-thiolate protected Au_{25} NCs (Fig. 5c) exhibit very similar or slightly improved parities compared to the fully protected NC, when all three adsorbates are present on the S or Au active sites. This indicates that the adsorbates may play the role of the stabilizing ligand by either maintaining or enhancing the energy balance between the SCBE and core CE of the

adsorbate-thiolate-protected Au_{25} NC. Regarding the stabilization of the partially protected Au_{25} NC, we observe that the CO and COOH intermediates present on the Au active site decrease the deviation from 1.02 kcal mol^{-1} (fully protected) to 0.67 kcal mol^{-1} and 0.55 kcal mol^{-1} (adsorbate-thiolate protected). These results are an important first step in confirming previous experimental and theoretical work that discuss the activity and robustness of the Au_{25} NC observed during the electrochemical reduction of CO_2 to CO [21, 22].

In order to obtain a more accurate understanding of the stability of the Au_{25} NC during experiments and to validate the stability results with the simplified SCH_3 ligands, we go one step further and use the $[Au_{25}(PET)_{18}]^{1-}$ crystal structure (PET = SCH_2CH_2Ph or phenylethanethiolate) to calculate the deviation of the Au_{25} NCs from parity before and after –R (CH_2CH_2Ph) or –SR (SCH_2CH_2Ph) ligand removal. PET is one of the most common organic molecules used to stabilize the $[Au_{25}(SR)_{18}]^{1-}$ NC [47]. As before, we used the TSM to assess the stability of the partially protected $[Au_{25}S(PET)_{17}]^{1-}$ and $[Au_{25}(PET)_{17}]^{1-}$ NCs. The results shown in Fig. 6 demonstrate that, upon ligand removal,
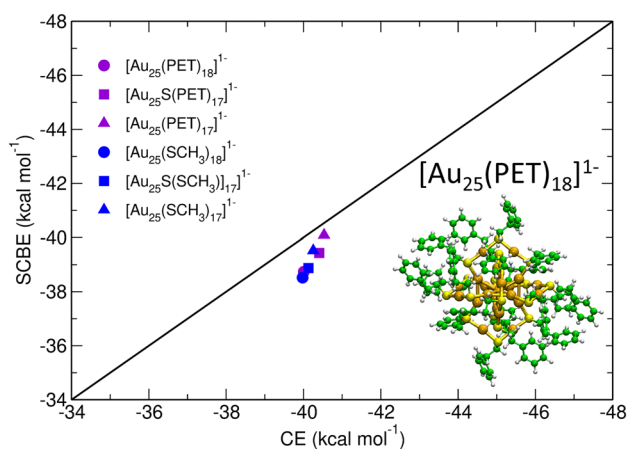
Fig. 6 Parity plot between shell-to-core binding energy (SCBE) and core cohesive energy (CE) upon –R or –SR removal for the $[Au_{25}(SR)_{18}]^{1-}$ NCs where SR = SCH_3 (blue) or PET (purple). Shapes indicate the different NCs upon ligand removal. The structure of the $[Au_{25}(PET)_{18}]^{1-}$ is shown as inset

Fig. 7 Deviation from parity $[Au_{25}SY(PET)_{17}]^{1-}$ and $[Au_{25}Y(PET)_{17}]^{1-}$ NCs compared to the original $[Au_{25}(PET)_{18}]^{1-}$ NC. In $[Au_{25}SY(PET)_{17}]^{1-}$ and $[Au_{25}Y(PET)_{17}]^{1-}$ the Y adsorbate is bonded to a S and Au active site, respectively

the PET-protected Au_{25} NCs follow similar trends as the Au_{25} NCs with the simplified ligands. This is a further evidence that the use of SCH_3 as model ligands to evaluate stability trends is valid. Moreover, the SCBE-CE energy balance (parity) of partially protected $[Au_{25}S(PET)_{17}]^{1-}$ and $[Au_{25}(PET)_{17}]^{1-}$ NCs remain practically unaffected (move slightly closer to parity) as compared to the original $[Au_{25}(PET)_{18}]^{1-}$ NC. This trend reiterates that it is indeed possible to generate a relatively stable partially protected NC with either a S or Au atom exposed on the NC surface. It is also worth noting that the Au_{25} NC has two different sites through which the S or Au atom can be exposed (see Supporting Info, Figure S1). Site 'A' denotes a site that consists of one Au shell atom and one Au core atom connected to a S atom to form the Au–SR–Au unit while Site 'B' denotes a site that consists of two Au shell atoms connected to a S atom to form the Au–SR–Au unit. We find that removal of the –SR group thermodynamically requires more energy than the removal of the –R group from either site on the Au_{25} NC (Fig. S1 and S2).

In a similar way as for the methylthiolate-protected NCs, after examining the stability of the partially protected $[Au_{25}S(PET)_{17}]^{1-}$ and $[Au_{25}(PET)_{17}]^{1-}$ NCs with respect to the original $[Au_{25}(PET)_{18}]^{1-}$ NC we calculate the deviation of the adsorbate-thiolate-protected $[Au_{25}SY(PET)_{17}]^{1-}$ and $[Au_{25}Y(PET)_{17}]^{1-}$ NCs from parity (with Y = H, CO, or COOH). In Fig. 7 we plot the deviation of the $[Au_{25}SY(PET)_{17}]^{1-}$ and $[Au_{25}Y(PET)_{17}]^{1-}$ NCs from parity along with that of the original $[Au_{25}(PET)_{18}]^{1-}$ NC. From Fig. 5c, we found that for the methylthiolate-protected Au_{25} NC, the smallest deviations in the parity are obtained for the $[Au_{25}Y(SCH_3)_{17}]^{1-}$ NCs (Y = H, CO, COOH). This trend is similar to the one observed in Fig. 7, once

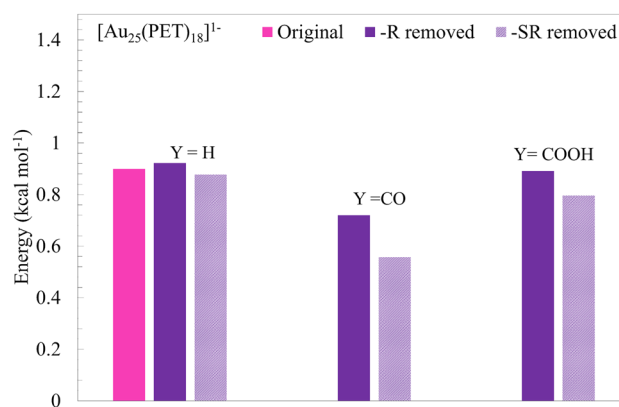again validating the use of -SCH_3 ligands instead of PET ligands to assess the stability of the Au_{25} NC using the TSM. The smallest deviations in the parity of the adsorbate-PET-protected Au_{25} NCs are found when the COOH and CO intermediates are adsorbed on the Au active site. This indicates that the adsorption of the COOH and CO intermediate preferably stabilizes the NC when it is present on the Au active site. Overall, Fig. 7 indicates that in all cases, the deviation from the parity is smaller than 1 kcal/mol, demonstrating that the removal of a ligand and adsorption of CO_2 reduction intermediates does not affect the overall stability of the NC. This is an important observation since it confirms the stability of the PET-protected Au_{25} NC as a catalyst for the electrochemical reduction of CO_2 [21, 22]. Furthermore, to address multiple ligand removal effects, we chose to remove 3 –SR groups from either site 'A' or site 'B' and 6 –SR groups from symmetric and asymmetric positions of the $[Au_{25}(PET)_{18}]^{1-}$ NC, which corresponds to 1/6 and 1/3 ligand loss from the surface of the NC (see Fig. S3 in the Supporting Information file). We chose to investigate the –SR removal since we expect to more dramatically affect the stability of the NC as it destroys the staple motifs on the NC surface (whereas –R removal leaves the sulfur atoms on the surface and the NC retains the staple motifs). The energetic SCBE-CE parity of the resulting Au_{25} NCs was analyzed using the TSM (Fig S4). Overall, we observe that as the number of –SR groups are removed, the deviation from parity gradually increases. Interestingly, when we adsorbed CO molecules on the sites of the NC that lost 6 ligands the deviation from parity exhibited by the $[Au_{25}CO_6(PET)_{12}]^{1-}$ NC is smaller compared to the $[Au_{25}(PET)_{12}]^{1-}$. This result clearly demonstrates the role of CO_2 reduction intermediates as stabilizing surface groups of the Au_{25} NC. Overall, the results presented in Figs. 3, 5, 6 and 7, clearly demonstrate that the Au_{25} NC retains its

stability upon ligand removal and adsorption of the CO_2 reduction intermediates.

In order to guide experimental detection of the CO_2 reduction intermediates, we calculate the absorption spectra of the original $[Au_{25}(PET)_{18}]^{1-}$ NC and the adsorbate-PET-protected structures with each of the reduction intermediates present on the S or Au active site of the partially protected NC (Fig. 8). The absorption spectrum calculation for the $[Au_{25}SCO(PET)_{17}]^{1-}$ was omitted since the CO was found to be the only molecule that does not chemisorb on the S active site (resulting to very similar energy parity behavior between the $[Au_{25}S(PET)_{17}]^{1-}$ and the $[Au_{25}SCO(PET)_{17}]^{1-}$; see Figs. 6 and 7). The comparison between the photoabsorption of the partially protected $[Au_{25}SY(PET)_{17}]^{1-}$ and $[Au_{25}Y(PET)_{17}]^{1-}$ NCs with respect to $[Au_{25}(PET)_{18}]^{1-}$ shows that the most drastic changes in lowest-energy regime of the spectra occur when the COOH and CO intermediate are present on the Au active site of the partially protected $[Au_{25}Y(PET)_{17}]^{1-}$ NCs (denoted by $[Au_{25}COOH(PET)_{17}]^{1-}$ and $[Au_{25}CO(PET)_{17}]^{1-}$ respectively). Particularly, we found that in the case of $[Au_{25}COOH(PET)_{17}]^{1-}$ and $[Au_{25}CO(PET)_{17}]^{1-}$ the lowest-energy peak (i.e. ≈ 1.2–1.5 eV), which is associated with metal-to-metal electronic transitions, redshifts by ≈ 0.1 eV with respect to $[Au_{25}(PET)_{18}]^{1-}$. According to the atomic charge analysis, the red-shifting of the lowest-energy peaks in the spectrum of $[Au_{25}COOH(PET)_{17}]^{1-}$ and $[Au_{25}CO(PET)_{17}]^{1-}$ is due to the changes in the atomic charges of the Au atoms of the Au_{25} core. Table S1, shows that the charges of the Au atoms that are directly bonded
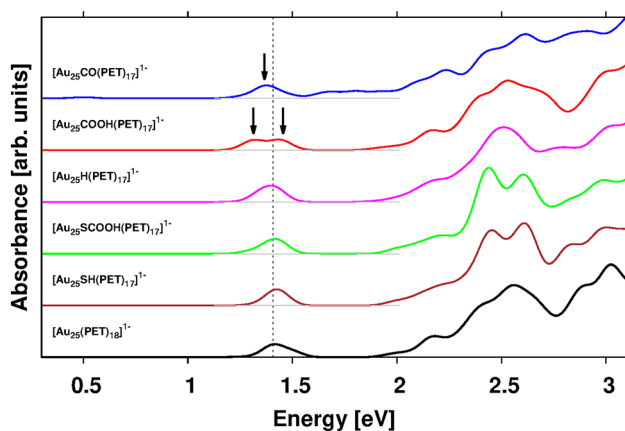
to CO and COOH are more positive (0.14 a. u.) than the rest of Au atoms of the staple motifs (0.08–0.09 a. u.). These results indicate that the CO and COOH adsorbates act as electron withdrawing groups when bonded directly to an Au active site. In contrast, when COOH is adsorbed on the surface of Au_{25} NCs through a S active site, the charges of the Au atoms of the Au_{25} core are similar to the ones found in the $[Au_{25}(PET)_{18}]^{1-}$ NC. This explains the similarity between the lowest-energy part of the spectra of $[Au_{25}SCOOH(PET)_{17}]^{1-}$ and $[Au_{25}(PET)_{18}]^{1-}$.

In Fig. 9, we compare the lowest photoabsorption peaks of the spectra of $[Au_{25}(PET)_{18}]^{1-}$ and the nanoclusters with the COOH intermediate on the Au and S active site. Although the lowest-part of the spectrum of $[Au_{25}SCOOH(PET)_{17}]^{1-}$ (≈ 1.2–1.5 eV) is similar to $[Au_{25}(PET)_{18}]^{1-}$, the type of electronic transitions occurring within this energy regime in these two clusters are different (see Table S2). In the latter case the electronic transitions between HOMO → LUMO occur at 1.21 eV, whereas in the spectrum of $[Au_{25}SCOOH(PET)_{17}]^{1-}$ they occur at energies > 1.24 eV. Moreover, the principal oscillator strengths associated to the electronic transitions between HOMO → LUMO in the spectrum of $[Au_{25}SCOOH(PET)_{17}]^{1-}$ (indicated with asterisk in Fig. 9 c) are at least one order of magnitude larger than in $[Au_{25}(PET)_{18}]^{1-}$ (see Table S2). Furthermore, in the case of $[Au_{25}COOH(PET)_{17}]^{1-}$ the lowest-energy absorption peak splits into two; one peak at 1.3 eV arising mainly from the electronic transitions between HOMO → LUMO, and a second peak at 1.4 eV which is mainly formed by the electronic transitions between the HOMO-1/HOMO-2 → LUMO + 1 (see Table S2). According to the shape of the Kohn–Sham molecular orbitals shown in Fig. 9d, e, the LUMOs of $[Au_{25}COOH(PET)_{17}]^{1-}$ and $[Au_{25}SCOOH(PET)_{17}]^{1-}$ are considerably determined by the local states of the COOH group. Therefore, we attribute the enhancement of the HOMO → LUMO transitions of the spectra of $[Au_{25}SCOOH(PET)_{17}]^{1-}$ and $[Au_{25}COOH(PET)_{17}]^{1-}$ to the presence of the local states of the COOH intermediate. Although thermodynamics indicate that the exposure of S upon ligand loss may be more feasible than Au (Fig. 2), the spectroscopic (photoabsorption) detection of adsorbed reaction intermediates on S-exposed sites appears more challenging than on Au on the low-energy absorption peaks (Fig. 8). An important point to note is that at higher energy (i.e. between 2.0 and 2.7 eV) the spectra of the $[Au_{25}SY(PET)_{17}]^{1-}$ and $[Au_{25}Y(PET)_{17}]^{1-}$ NCs change notably in comparison to the spectrum of $[Au_{25}(PET)_{18}]^{1-}$. Within this energy window, the absorption spectrum becomes rather complex and the shape of the higher-energy absorption peaks is largely determined by electronic transitions between the local d states of Au and the states of the protecting layer [48].

Fig. 8 Absorption spectra of $[Au_{25}(PET)_{18}]^{1-}$ (black), $[Au_{25}SH(PET)_{17}]^{1-}$ (brown), $[Au_{25}SCOOH(PET)_{17}]^{1-}$ (green), $[Au_{25}H(PET)_{17}]^{1-}$ (pink), $[Au_{25}COOH(PET)_{17}]^{1-}$ (red), and $[Au_{25}CO(PET)_{17}]^{1-}$ (blue). Dashed line at 1.41 eV is used as a reference to indicate the lowest-energy absorption peak of $[Au_{25}(PET)_{18}]^{1-}$ and visualize red or blue shifting of this peak in the spectra of the $[Au_{25}SY(PET)_{17}]^{1-}$ and $[Au_{25}Y(PET)_{17}]^{1-}$ NCs. Arrows indicate the red-shifting and splitting of the lowest-energy transitions of the $[Au_{25}COOH(PET)_{17}]^{1-}$ and $[Au_{25}CO(PET)_{17}]^{1-}$

Fig. 9 Comparison of the lowest-energy absorption peaks of $[Au_{25}COOH(PET)_{17}]^{1-}$ (**a**), $[Au_{25}SCOOH(PET)_{17}]^{1-}$ (**b**), and $[Au_{25}(PET)_{18}]^{1-}$ (**c**), along with their corresponding HOMO and LUMO states (**d**–**f**). The vertical lines in the spectra correspond to the single oscillator strengths relative to individual electronic transitions. The asterisks indicate the oscillator strengths with the largest contributions from HOMO→LUMO transitions. Black circles in (**d**), (**e**), and (**f**), indicate the position of the COOH group and its local electronic states
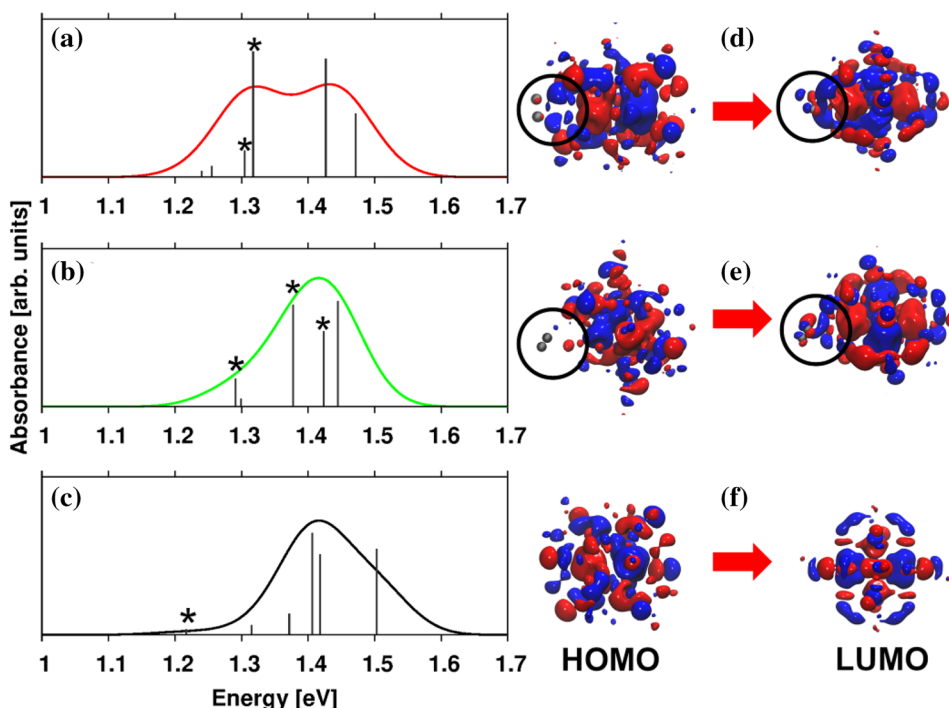
In order to identify any changes in the ligand structure during CO_2 reduction reaction, ex situ UV–Vis absorption and Raman spectroscopy measurements were carried out for $[Au_{25}(PET)_{18}]^{1-}$ before and after electrochemical reduction of CO_2 at − 1.0 V versus RHE. The UV–Vis absorption spectra in Fig. 10a match well with previously reported, energy-dependent spectra of room-temperature $[Au_{25}(PET)_{18}]^{1-}$ NC [44, 45], and the UV–Vis experimental results indicate that the NC absorption spectrum remains essentially unaltered after CO_2 reduction (Fig. 10a and S5a). Since the $[Au_{25}(PET)_{18}]^{1-}$ NC is active for CO_2 reduction [22]

and the activity has been attributed to sites that have lost ligands [17, 21, 31], we believe that the absorption spectra probes an ensemble of different states of the NC, involving states with adsorbed reduction intermediates (on the sites that lost ligands). In fact, our TDDFT calculations demonstrate that the spectra of the $[Au_{25}SY(PET)_{17}]^{1-}$ nanoclusters (from S exposure) resemble the absorption features of $[Au_{25}(PET)_{18}]^{1-}$ at energy below 2.2 eV. Since beyond this energy the calculated spectra become complex (many electronic transitions involving ligands), only the lowest-energy absorption peaks can be reliably used to
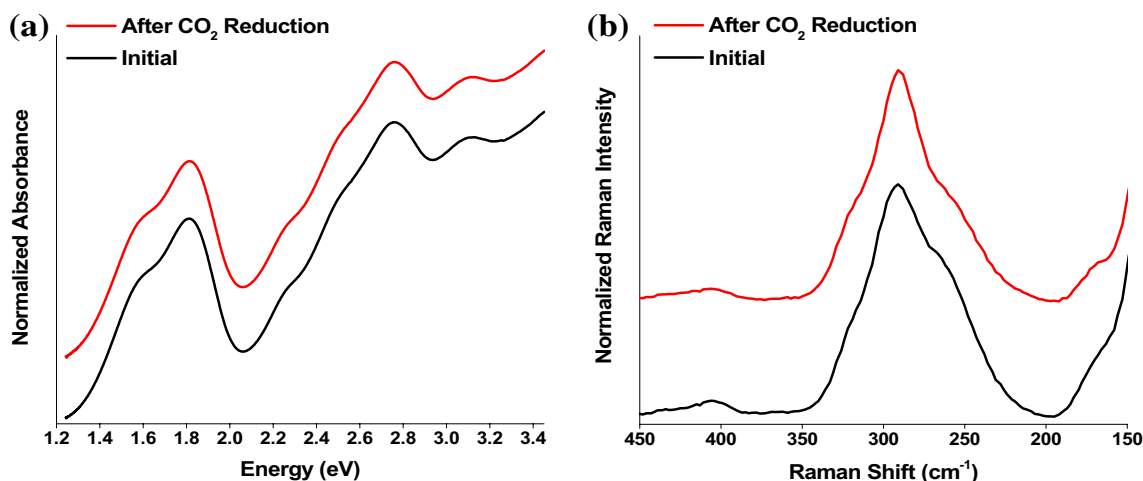

Fig. 10 a UV–Vis absorption spectra and **b** Raman spectra of $[Au_{25}(PET)_{18}]^{1-}$ nanoclusters before (solid black line) and after (solid red line) electrochemical CO_2 reduction. The normalized spectra were offset for clarity

make an accurate comparison between the experimental and calculated spectra. In addition, taking into account that the largest changes observed by TDDFT calculations in the lowest-energy absorption peaks were for the $[Au_{25}Y(PET)_{17}]^{1-}$ nanoclusters (Figs. 8 and 9), the experimental results in Fig. 10a suggest that species in which an Au atom is directly bonded to an adsorbate (Au exposure), are less probable to exist than $[Au_{25}SY(PET)_{17}]^{1-}$. This also fully agrees with the thermodynamic preference of removing –R versus –SR under electrochemical conditions (Fig. 2).

Experimental, ex situ Raman spectroscopy was also conducted to probe changes in vibrational modes associated with gold-thiol units in the ligand shell of $[Au_{25}(PET)_{18}]^{1-}$ [3, 49, 50]. The Raman spectra in Fig. 10b are consistent with previous experimental and theoretical reports of thiol-protected nanoclusters [49, 50], and the identical peak energies and similar spectral shapes indicate a majority of the Au–S bonds are retained after electrochemical CO_2 reduction. Subtle changes in the overlaid peak shapes between 200 and 350 cm^{-1} might be a consequence of a change in Au–S vibrational modes after the CO_2 reduction reaction experiment (Figure S5b). This could be attributed to replacing organic ligands (-R) with CO_2 reduction intermediates, but the presence of multiple overlapping vibrational modes in this spectral region [50] make definitive assignment of specific structural changes difficult. Although, thermodynamics, stability and absorption spectra analysis (both theoretical and experimental) suggest the $[Au_{25}SY(PET)_{17}]^{1-}$ nanoclusters to be probable species formed during the electrochemical reduction of CO_2, it is a challenge to identify the type of reaction intermediates (Y) present on the surface through UV–Vis analysis. A molecular-level fingerprinting analysis, such as in situ IR, could potentially resolve this challenge in future research steps.

5　Conclusions

Using first principles calculations, we analyzed the stability of $[Au_{18}(SR)_{14}]^0$, $[Au_{23}(SR)_{16}]^{1-}$, $[Au_{25}(SR)_{18}]^{1-}$, and $[Au_{28}(SR)_{20}]^0$ NCs upon ligand removal, which has been found to be an important step for converting a NC to an active catalyst for CO_2 electroreduction [17, 31]. In particular, we calculated the reaction energy of removing a single –R or –SR group from the protecting layer of the NCs (assuming reduction reactions) to generate a surface S or Au site as active site for catalysis. We found that for all the NCs, removing the –R group is thermodynamically more favorable than removing a –SR group. Particularly, we found that the removal of a –R group from the $[Au_{25}(SR)_{18}]^{1-}$ NC (and exposure of surface S-site)

is most favorable compared to the other three NCs. We also analyzed the stability of the partially protected Au NCs using the thermodynamic stability model (TSM) [11]. Our results demonstrate the thermodynamic stability of the $[Au_{25}(SR)_{18}]^{1-}$ NC even after ligand removal to $[Au_{25}S(SR)_{17}]^{1-}$ and $[Au_{25}(SR)_{17}]^{1-}$, exhibiting exposed S and Au active sites, respectively. Furthermore, we show that the partially-protected Au$_{25}$ NC remains stable upon adsorption of the electrochemical CO_2 reduction reaction intermediates (H, CO and COOH) on the generated S or Au active sites and this NC is more stable than the rest (Au$_{18}$, Au$_{23}$ and Au$_{28}$ NCs). In addition, TDDFT calculations reveal that adsorption of the COOH and CO reaction intermediates on an Au active site leads to a slight modification (red-shifting) of the lowest-energy peak when compared to the spectrum of $[Au_{25}(PET)_{18}]^{1-}$, whereas adsorption on S active sites does not alter the main absorption features. UV–Vis experimental measurements on $[Au_{25}(PET)_{18}]^{1-}$ before and after CO_2 electrochemical reduction did not reveal any changes in the photoabsorption spectra, suggesting that S-exposure is probable under electrochemical conditions, a fact that was verified by Raman spectroscopy (change in the Au–S vibrational modes due to adsorption of CO_2 reduction intermediates on S-sites). These results explain the high activity (due to S exposure) and stability of the Au$_{25}$ ligand-protected NC under CO_2 electrochemical reduction conditions.

Compliance with ethical standards

Conflict of interest On behalf of all authors, the corresponding author states that there is no conflict of interest.

References

1. Jin R, Zeng C, Zhou M, Chen Y (2016) Atomically precise colloidal metal nanoclusters and nanoparticles: fundamentals and opportunities. Chem Rev 116(18):10346–10413. https://doi.org/10.1021/acs.chemrev.5b00703

2. Knoppe S, Hakkinen H, Verbiest T (2015) Nonlinear optical properties of thiolate-protected gold clusters: a theoretical survey of the first hyperpolarizabilities. J Phys Chem C 119(49):27676–27682. https://doi.org/10.1021/acs.jpcc.5b08341

3. Qian H, Zhu Y, Jin R (2012) Atomically precise gold nanocrystal molecules with surface plasmon resonance. Proc Natl Acad Sci USA 109(3):696–700. https://doi.org/10.1073/pnas.1115307109

4. Cowan MJ, Mpourmpakis G (2019) Structure–property relationships on thiolate-protected gold nanoclusters. Nanoscale Adv. https://doi.org/10.1039/c8na00246k

5. Jin R (2010) Quantum sized, thiolate-protected gold nanoclusters. Nanoscale 2(3):343–362. https://doi.org/10.1039/B9NR00160C

6. Jadzinsky PD, Calero G, Ackerson CJ, Bushnell DA, Kornberg RD (2007) Structure of a thiol monolayer-protected gold nanoparticle at 1.1 Å resolution. Science 318(5849):430. https://doi.org/10.1126/science.1148624

7. Walter M, Akola J, Lopez-Acevedo O, Jadzinsky PD, Calero G, Ackerson CJ, Whetten RL, Grönbeck H, Häkkinen H (2008) A unified view of ligand-protected gold clusters as superatom complexes. Proc Natl Acad Sci 105(27):9157. https://doi.org/10.1073/pnas.0801001105

8. Zeng C, Liu C, Chen Y, Rosi NL, Jin R (2014) Gold-thiolate ring as a protecting motif in the $Au_{20}(SR)_{16}$ nanocluster and implications. J Am Chem Soc 136(34):11922–11925. https://doi.org/10.1021/ja506802n

9. Häkkinen H, Walter M, Grönbeck H (2006) Divide and protect: capping gold nanoclusters with molecular gold–thiolate rings. J Phys Chem B 110(20):9927–9931. https://doi.org/10.1021/jp0619787

10. Das A, Liu C, Zeng C, Li G, Li T, Rosi NL, Jin R (2014) Cyclopentanethiolato-protected $Au_{36}(SC5H9)_{24}$ nanocluster: crystal structure and implications for the steric and electronic effects of ligand. J Phys Chem A 118(37):8264–8269. https://doi.org/10.1021/jp501073a

11. Taylor MG, Mpourmpakis G (2017) Thermodynamic stability of ligand-protected metal nanoclusters. Nat Commun 8:15988. https://doi.org/10.1038/ncomms15988

12. Kauffman DR, Alfonso D, Matranga C, Ohodnicki P, Deng X, Siva RC, Zeng C, Jin R (2014) Probing active site chemistry with differently charged $Au_{25}q$ nanoclusters (q = − 1, 0, +1). Chem Sci. https://doi.org/10.1039/c4sc00997e

13. Jin R, Higaki T, Li Y, Zhao S, Li Q, Li S, Du X, Yang S, Chai J (2019) Atomically tailored gold nanoclusters for catalytic application. Angew Chem Int Ed Engl. https://doi.org/10.1002/anie.201814156

14. Kogo A, Sakai N, Tatsuma T (2010) Photocatalysis of Au_{25}-modified TiO_2 under visible and near infrared light. Electrochem Commun 12(7):996–999. https://doi.org/10.1016/j.elecom.2010.05.021

15. Wang YG, Yoon Y, Glezakou VA, Li J, Rousseau R (2013) The role of reducible oxide-metal cluster charge transfer in catalytic processes: new insights on the catalytic mechanism of CO oxidation on Au/TiO_2 from ab initio molecular dynamics. J Am Chem Soc 135(29):10673–10683. https://doi.org/10.1021/ja402063v

16. Yu C, Li G, Kumar S, Kawasaki H, Jin R (2013) Stable $Au_{25}(SR)_{18}$/TiO_2 composite nanostructure with enhanced visible light photocatalytic activity. J Phys Chem Lett 4(17):2847–2852. https://doi.org/10.1021/jz401447w

17. Zhao S, Austin N, Li M, Song Y, House SD, Bernhard S, Yang JC, Mpourmpakis G, Jin R (2018) Influence of atomic-level morphology on catalysis: the case of sphere and rod-like gold nanoclusters for CO_2 electroreduction. ACS Catal 8(6):4996–5001. https://doi.org/10.1021/acscatal.8b00365

18. Li G, Jin R (2014) Gold nanocluster-catalyzed semihydrogenation: a unique activation pathway for terminal alkynes. J Am Chem Soc 136(32):11347–11354. https://doi.org/10.1021/ja503724j

19. Li G, Qian H, Jin R (2012) Gold nanocluster-catalyzed selective oxidation of sulfide to sulfoxide. Nanoscale 4(21):6714–6717. https://doi.org/10.1039/c2nr32171h

20. Negishi Y, Mizuno M, Hirayama M, Omatoi M, Takayama T, Iwase A, Kudo A (2013) Enhanced photocatalytic water splitting by $BaLa_4Ti_4O_{15}$ loaded with approximately 1 nm gold nanoclusters using glutathione-protected Au_{25} clusters. Nanoscale 5(16):7188–7192. https://doi.org/10.1039/c3nr01888a

21. Austin N, Zhao S, McKone JR, Jin R, Mpourmpakis G (2018) Elucidating the active sites for CO_2 electroreduction on ligand-protected Au_{25} nanoclusters. Catal Sci Technol 8(15):3795–3805. https://doi.org/10.1039/c8cy01099d

22. Kauffman DR, Thakkar J, Siva R, Matranga C, Ohodnicki PR, Zeng C, Jin R (2015) Efficient electrochemical CO2 conversion powered by renewable energy. ACS Appl Mater Interfaces 7(28):15626–15632. https://doi.org/10.1021/acsami.5b04393

23. Wu Z, Hu G, Jiang DE, Mullins DR, Zhang QF, Allard LF Jr, Wang LS, Overbury SH (2016) Diphosphine-protected Au_{22} nanoclusters on oxide supports are active for gas-phase catalysis without ligand removal. Nano Lett. https://doi.org/10.1021/acs.nanolett.6b03221

24. Ma L, Melander M, Weckman T, Laasonen K, Akola J (2016) CO Oxidation on the $Au_{15}Cu_{15}$ cluster and the role of vacancies in the MgO(100) support. J Phys Chem C 120(47):26747–26758. https://doi.org/10.1021/acs.jpcc.6b06876

25. Nie X, Qian H, Ge Q, Xu H, Jin R (2012) CO oxidation catalyzed by oxide-supported $Au_{25}(SR)_{18}$ nanoclusters and identification of perimeter sites as active centers. ACS Nano 6(7):6014–6022. https://doi.org/10.1021/nn301019f

26. Kauffman DR, Alfonso D, Matranga C, Qian H, Jin R (2012) Experimental and computational investigation of Au_{25} clusters and CO_2: a unique interaction and enhanced electrocatalytic activity. J Am Chem Soc 134(24):10237–10243. https://doi.org/10.1021/ja303259q

27. Wu Z, Jiang DE, Mann AK, Mullins DR, Qiao ZA, Allard LF, Zeng C, Jin R, Overbury SH (2014) Thiolate ligands as a double-edged sword for CO oxidation on CeO_2 supported $Au_{25}(SCH2CH2Ph)_{18}$ nanoclusters. J Am Chem Soc 136(16):6111–6122. https://doi.org/10.1021/ja5018706

28. Shivhare A, Ambrose SJ, Zhang H, Purves RW, Scott RW (2013) Stable and recyclable Au_{25} clusters for the reduction of 4-nitrophenol. Chem Commun (Camb) 49(3):276–278. https://doi.org/10.1039/c2cc37205c

29. Li G, Abroshan H, Chen Y, Jin R, Kim HJ (2015) Experimental and mechanistic understanding of aldehyde hydrogenation using Au_{25} nanoclusters with lewis acids: unique sites for catalytic reactions. J Am Chem Soc 137(45):14295–14304. https://doi.org/10.1021/jacs.5b07716

30. Zhu Y, Qian H, Drake BA, Jin R (2010) Atomically precise $Au_{25}(SR)_{18}$ nanoparticles as catalysts for the selective hydrogenation of alpha, beta-unsaturated ketones and aldehydes. Angew Chem Int Ed Engl 49(7):1295–1298. https://doi.org/10.1002/anie.200906249

31. Alfonso DR, Kauffman D, Matranga C (2016) Active sites of ligand-protected Au_{25} nanoparticle catalysts for CO_2 electroreduction to CO. J Chem Phys 144(18):184705. https://doi.org/10.1063/1.4948792

32. Perdew JP, Burke K, Ernzerhof M (1996) Generalized gradient approximation made simple. Phys Rev Lett 77(18):3865–3868. https://doi.org/10.1103/PhysRevLett.77.3865

33. VandeVondele J, Hutter J (2007) Gaussian basis sets for accurate calculations on molecular systems in gas and condensed phases. J Chem Phys 127(11):114105. https://doi.org/10.1063/1.2770708

34. VandeVondele J, Krack M, Mohamed F, Parrinello M, Chassaing T, Hutter J (2005) Quickstep: fast and accurate density functional calculations using a mixed Gaussian and plane waves approach. Comput Phys Commun 167(2):103–128. https://doi.org/10.1016/j.cpc.2004.12.014

35. MacDonald MA, Chevrier DM, Zhang P, Qian H, Jin R (2011) The structure and bonding of $Au_{25}(SR)_{18}$ nanoclusters from EXAFS: the interplay of metallic and molecular behavior. J Phys Chem C 115(31):15282–15287. https://doi.org/10.1021/jp204922m

36. Das A, Li T, Nobusada K, Zeng C, Rosi NL, Jin R (2013) Nonsuperatomic $[Au_{23}(SC6H11)_{16}]$-nanocluster featuring bipyramidal Au_{15} kernel and trimeric $Au_3(SR)_4$ motif. J Am Chem Soc 135(49):18264–18267. https://doi.org/10.1021/ja409177s

37. Das A, Liu C, Byun HY, Nobusada K, Zhao S, Rosi N, Jin R (2015) Structure determination of $[Au_{18}(SR)_{14}]$. Angew Chem Int Ed Engl 54(10):3140–3144. https://doi.org/10.1002/anie.201410161

38. Zeng C, Li T, Das A, Rosi NL, Jin R (2013) Chiral structure of thiolate-protected 28-gold-atom nanocluster determined by X-ray crystallography. J Am Chem Soc 135(27):10011–10013. https://doi.org/10.1021/ja404058q

39. Das S, Goswami A, Hesari M, Al-Sharab JF, Mikmekova E, Maran F, Asefa T (2014) Reductive deprotection of monolayer protected nanoclusters: an efficient route to supported ultrasmall au nanocatalysts for selective oxidation. Small 10(8):1473–1478. https://doi.org/10.1002/smll.201302854

40. Nasaruddin RR, Chen T, Yan N, Xie J (2018) Roles of thiolate ligands in the synthesis, properties and catalytic application of gold nanoclusters. Coord Chem Rev 368:60–79. https://doi.org/10.1016/j.ccr.2018.04.016

41. Fang Y, Cheng X, Flake JC, Xu Y (2019) CO_2 electrochemical reduction at thiolate-modified bulk Au electrodes. Catal Sci Technol 9(10):2689–2701. https://doi.org/10.1039/C9CY00506D

42. Mortensen JJ, Hansen LB, Jacobsen KW (2005) Real-space grid implementation of the projector augmented wave method. Phys Rev B 71(3):035109. https://doi.org/10.1103/PhysRevB.71.035109

43. Enkovaara J, Rostgaard C, Mortensen JJ, Chen J, Dułak M, Ferrighi L, Gavnholt J, Glinsvad C, Haikola V, Hansen HA, Kristoffersen HH, Kuisma M, Larsen AH, Lehtovaara L, Ljungberg M, Lopez-Acevedo O, Moses PG, Ojanen J, Olsen T, Petzold V, Romero NA, Stausholm-Møller J, Strange M, Tritsaris GA, Vanin M, Walter M, Hammer B, Häkkinen H, Madsen GKH, Nieminen RM, Nørskov JK, Puska M, Rantala TT, Schiøtz J, Thygesen KS, Jacobsen KW (2010) Electronic structure calculations with GPAW: a real-space implementation of the projector augmented-wave method. J Phys Condens Matter 22(25):253202. https://doi.org/10.1088/0953-8984/22/25/253202

44. Negishi Y, Nobusada K, Tsukuda T (2005) Glutathione-protected gold clusters revisited: bridging the gap between gold(I)–thiolate complexes and thiolate-protected gold nanocrystals. J Am Chem Soc 127:5261–5270. https://doi.org/10.1021/ja042218h

45. Devadas MS, Bairu S, Qian H, Sinn E, Jin R, Ramakrishna G (2011) Temperature-dependent optical absorption properties of monolayer-protected Au_{25} and Au_{38} clusters. J Phys Chem Lett 2:2752–2758. https://doi.org/10.1021/jz2012897

46. Austin N, Zhao S, McKone JR, Jin R, Mpourmpakis G (2018) Elucidating the active sites for CO_2 electroreduction on ligand-protected Au_{25} nanoclusters. Catal Sci Technol. https://doi.org/10.1039/C8CY01099D

47. Kang X, Chong H, Zhu M (2018) $Au_{25}(SR)_{18}$: the captain of the great nanocluster ship. Nanoscale 10(23):10758–10834. https://doi.org/10.1039/C8NR02973C

48. Juarez-Mosqueda R, Mpourmpakis G (2019) Elucidating the optical spectra of $[Au_{25}(SR)_{18}]q$ nanoclusters. Phys Chem Chem Phys 21(40):22272–22282. https://doi.org/10.1039/C9CP03982A

49. Parker JF, Choi J-P, Wang W, Murray RW (2008) Electron self-exchange dynamics of the nanoparticle couple $[Au_{25}(SC_2Ph)_{18}]^{0/1-}$ by nuclear magnetic resonance line-broadening. J Phys Chem C 112:13976–13981. https://doi.org/10.1021/jp805638x

50. Varnholt B, Oulevey P, Luber S, Kumara C, Dass A, Bürgi T (2014) Structural information on the Au–S interface of thiolate-protected gold clusters: a Raman spectroscopy study. J Phys Chem C 118:9604–9611. https://doi.org/10.1021/jp502453q